Supplement of Atmos. Chem. Phys., 26, 6427–6448, 2026
https://doi.org/10.5194/acp-26-6427-2026-supplement

Atmospheric Chemistry and Physics
Open Access

Supplement of

A modeling study of global distribution and formation pathways of highly oxygenated organic molecules (HOMs) from monoterpenes

Xinyue Shao et al.

Correspondence to: Xinyi Dong (dongxy@nju.edu.cn) and Minghuai Wang (minghuai.wang@nju.edu.cn)

Text S1.

The formation, photolysis, scavenging, and gas-particle partitioning processes of HOMs-SOA are detailed introduced as follows.

1. Monoterpene oxidation

The new branching which forms RO_2 that can undergo autoxidation are included in the original monoterpene + OH\$O_3$ reactions, as shown in Table S1 and S2. The HOMs-SOA formed by the initial oxidation between monoterpenes and NO_3 radical are not considered here because the branching ratio may be very low and remain large uncertainties (Roldin et al., 2019), although the NO_3-initiated HOMs-SOA are reported and may be significant in the nighttime (Nah et al., 2016; Yan et al., 2016). The $APINO_2$, $BPINO_2$, $LIMONO_2$, and $MYRCO_2$ are the original formed RO_2 that cannot form HOMs. Here we used high branching ratios in the generation of MT-bRO_2 as shown in Table S3 in Xu et al. (2022). The branching ratios of the yield of MT-aRO_2 to the yield of MT-bRO_2 ($f_{MT\text{-}aRO2}/f_{MT\text{-}bRO2}$) for the monoterpenes + OH reaction is 0.25:0.75. The $f_{MT\text{-}aRO2}/f_{MT\text{-}bRO2}$ for the monoterpenes + O_3 reaction is 0.92:0.08. All the branching ratios used here are within the ranged used in the previous studies. The yields range of MT-bRO_2 formed by monoterpenes + OH and monoterpenes + O_3 are 0.075 ~ 0.83 (Lee et al., 2023; Piletic and Kleindienst, 2022; Pye et al., 2019; Weber et al., 2020; Xu et al., 2019) and 0 ~ 0.22 (Ehn et al., 2014; Jokinen et al., 2015; Roldin et al., 2019), respectively. The reaction rate constants are the same as the default monoterpenes + OH\$O_3$ reactions.

Table S1. initial oxidation between monoterpenes and OH radical

Index	Reactions	Reaction rate
1	APIN + OH → 0.25*$APINO_2$ + 0.75*MT-bRO_2	1.34e-11*exp(410/T)
2	BPIN + OH → 0.25*$BPINO_2$ + 0.75*MT-bRO_2	1.62e-11*exp(460/T)
3	LIMON + OH → 0.25*$LIMONO_2$ + 0.75*MT-bRO_2	3.41e-11*exp(470/T)
4	MYRC + OH → 0.25*$MYRCO_2$ + 0.75*MT-bRO_2	2.1e-10

Table S2. initial oxidation between monoterpenes and O_3

Index	Reactions	Reaction rate
5	APIN + O_3 → 0.736*$APINO_2$ + 0.064*MT-bRO_2 + 0.77*OH + 0.066*$TERPA2O_2$ + 0.22*H_2O_2 + 0.044*TERPA + 0.002*TERPACID + 0.034*TERPA2 +	1.34e-11* exp(410/T)

	0.17*HO_2 + 0.17*CO + 0.27*CH_2O + 0.054*TERPA2CO_3	
6	BPIN + O_3 → 0.736*$BPINO_2$ + 0.064*MT-bRO_2 + 0.102*TERPK + 0.3*OH + 0.06*TERPA2CO_3 + 0.32*H_2O_2 + 0.038*BIGALK + 0.19*CO_2 + 0.81*CH_2O +0.11*HMHP + 0.08*HCOOH	1.62e-11* exp(460/T)
7	LIMON + O_3 → 0.736*$LIMONO_2$ + 0.064*MT-bRO_2 + 0.66*OH + 0.132*TERPF1 + 0.33*CH_3CO_3 + 0.33*CH_2O + 0.066*TERPA3CO_3 + 0.33*H_2O_2 + 0.002*TERPACID	3.41e-11* exp(470/T)
8	MYRC + O_3 → 0.736*$MYRCO_2$ + 0.064*MT-bRO_2 + 0.2*TERPF2 + 0.63*OH + 0.63*HO_2 + 0.25*CH_3COCH_3 +0.39*CH_2O + 0.18*HYAC	2.1e-10

2. Autoxidation

The MT-bRO_2 will undergo fast intramolecular reactions. The hydrogen-atom is shifted to form an alkyl radical where O_2 rapidly attaches to form a more oxidized RO_2 radical, which is called autoxidation. The MT-bRO_2 may go through several generations of autoxidation reaction. The autoxidation reactions of MT-bRO_2 are lumped into two generations as shown in Table S3, where the reaction rate is temperature-dependent (Berndt et al., 2016; Xu et al., 2022). The activation energies are 74.1 kJ/mol which are within in the range from previous studies (Lee et al., 2023; Moller et al., 2020; Pye et al., 2019; Roldin et al., 2019; Schervish and Donahue, 2020; Xu et al., 2019).

Table S3. autoxidation reaction

Index	Reactions	Reaction rate
9	MT-bRO_2 → MT-cRO_2	9.8e12*exp(-8836/T)
10	MT-cRO_2 → MT-HOM-RO_2	9.8e12*exp(-8836/T)

3. Self- and cross-reactions for accretion products

Due to isomers of MT-RO_2 and ISOP-RO_2, 64 self- and cross-reactions are added (Table S4), where three branches are considered for the products. First, the intermediate products are produced and are lumped as C_{10}-ROH and C_{10}-CBYL. Second, RO radicals are generated, and may produce HO_2 and C_{10}-CBYL or decompose into smaller compounds. Half of the RO are assumed to decompose into smaller carbonyls. Third, accretion products (SOAGac20 and SOAGac15) are produced. The branching ratios of the three pathways above were set as 0.29:0.67:0.04, respectively (Xu et al., 2022). However, for the self- and cross-reactions involving MT-aRO_2 ($APINO_2$, $BPINO_2$, $LIMONO_2$, and $MYRCO_2$) and ISOP-RO_2, a small fraction of RO radicals are possible to undergo a unimolecular H-shift to form MT-bRO_2, and the branching ratio are set to 0.05 (Xu et al., 2022). The fast reaction rate are applied here based on Table S4 in Xu et al. (2022).

Table S4. self- and cross-reactions to form gas-phase accretion products

Index	Reactions	Reaction rate
11–20	MT-aRO_2 + MT-aRO_2 → 0.893*C_{10}-CBYL + 0.29*C_{10}-ROH + 0.603*HO_2 + 1.34*HYDRALD + 0.067*MT-bRO_2 + 0.04*SOAGac20	4.0e-11
21–24	MT-aRO_2 + MT-bRO_2 → 0.96*C10-CBYL + 0.29*C10-ROH + 0.67*HO2 + 1.34*HYDRALD + 0.04*SOAGac20	4.0e-11
25–28	MT-aRO_2 + MT-cRO_2 → 0.96*C10-CBYL + 0.29*C10-ROH + 0.67*HO2 + 1.34*HYDRALD + 0.04*SOAGac20	2.6e-10
29–32	MT-aRO_2 + MT-HOM-RO_2 → 0.96*C10-CBYL + 0.29*C10-ROH + 0.67*HO2 + 1.34*HYDRALD + 0.04*SOAGac20	2.6e-10
33–56	MT-aRO_2 + ISOP-RO_2 → 0.4465*C10-CBYL + 0.145*C10-ROH + 0.145*ROH + 0.603*HO2 + 1.485*HYDRALD + 0.0335*MT-bRO2 + 0.04*SOAGac15	2.0e-11
57	MT-bRO_2 + MT-bRO_2 → 0.96*C_{10}-CBYL + 0.29*C_{10}-ROH + 0.67*HO_2 + 1.34*HYDRALD + 0.04*SOAGac20	4.0e-11
58	MT-cRO_2 + MT-cRO_2 → 0.96*C_{10}-CBYL + 0.29*C_{10}-ROH + 0.67*HO_2 + 1.34*HYDRALD + 0.04*SOAGac20	2.6e-10
59	MT-HOM-RO_2 + MT-HOM-RO_2 → 0.96*C_{10}-CBYL + 0.29*C_{10}-ROH + 0.67*HO_2 + 1.34*HYDRALD + 0.04*SOAGac20	2.6e-10
60	MT-bRO_2 + MT-cRO_2 → 0.96*C_{10}-CBYL + 0.29*C_{10}-ROH + 0.67*HO_2 + 1.34*HYDRALD + 0.04*SOAGac20	2.6e-10
61	MT-bRO_2 + MT-HOM-RO_2 → 0.96*C_{10}-CBYL + 0.29*C_{10}-ROH + 0.67*HO_2 + 1.34*HYDRALD + 0.04*SOAGac20	2.6e-10
62	MT-cRO_2 + MT-HOM-RO_2 → 0.96*C_{10}-CBYL + 0.29*C_{10}-ROH + 0.67*HO_2 + 1.34*HYDRALD + 0.04*SOAGac20	2.6e-10
63–68	MT-bRO_2 + ISOP-RO_2 → 0.48*C_{10}-CBYL + 0.145*C_{10}-ROH + 0.145*ROH + 0.67*HO_2 + 1.485*HYDRALD + 0.04*SOAGac15	2.0e-11
69–74	MT-cRO_2 + ISOP-RO_2 → 0.48*C_{10}-CBYL + 0.145*C_{10}-ROH + 0.145*ROH + 0.67*HO_2 + 1.485*HYDRALD + 0.04*SOAGac15	4.0e-11
75–80	MT-HOM-RO_2 + ISOP-RO_2 → 0.48*C_{10}-CBYL + 0.145*C_{10}-ROH + 0.145*ROH + 0.67*HO_2 + 1.485*HYDRALD + 0.04*SOAGac15	4.0e-11

4. MT-RO_2 reactions with methylperoxy/peroxyacetyl radicals

As shown in Table S5, the reactions between original MT-RO_2 and CH_3O_2/CH_3CO_3 are modified based on Xu et al. (2022) to consider the branch to form MT-bRO_2. The rate constants remain unchanged. When MT-bRO_2, MT-cRO_2, and MT-HOM-RO_2 are terminated by methylperoxy/peroxyacetyl radicals, C_{10}-ROH, C_{10}-CBYL, and some small molecules are generated. The rate constants are the same as Xu et al. (2022).

Table S5. MT-RO_2 reactions with methylperoxy/peroxyacetyl radicals

Index	Reactions	Reaction rate
81	$APINO_2 + CH_3CO_3 \rightarrow$ 0.05*MT-bRO_2 + 0.3705*TERPA + 0.3325*TERPA3 + 0.133*TERP1OOH + 0.12*CH_3COCH_3 + 0.114*TERPF1 + 0.27*CH_2O + HO_2 + CH_3O_2 + CO_2	2e-12* exp(500/T)
82	$APINO_2 + CH_3O_2 \rightarrow$ 0.05*MT-bRO_2 + 0.83*CH_2O + 0.133*TERPF1 + 0.399*TERPA + 0.19*TERPA3 + 0.1235*TERP1OOH + 0.17*CH_3OH + 0.1045*TERPK + 0.06*CH_3COCH_3 + 1.16*HO_2	2e-12
83	$BPINO_2 + CH_3CO_3 \rightarrow$ 0.05*MT-bRO_2 + 0.304*TERPK + 0.2565*TERPF1 + 0.3895*TERPA3 + 0.11*CH_3COCH_3 + 0.65*CH_2O + HO_2 + CH_3O_2 + CO_2	2e-12* exp(500/T)
84	$BPINO_2 + CH_3O_2 \rightarrow$ 0.05*MT-bRO_2 + 1.4*CH_2O + 0.3515*TERPF1 + 0.304*TERPK + 1.5*HO_2 + 0.08*CH_3COCH_3 + 0.2945*TERPA3	2e-12
85	$LIMONO_2 + CH_3CO_3 \rightarrow$ 0.05*MT-bRO_2 + 0.95*TERPF1 + 0.56*CH_2O + HO_2 + CH_3O_2 + CO_2	2e-12* exp(500/T)
86	$LIMONO_2 + CH_3O_2 \rightarrow$ 0.05*MT-bRO_2 + 0.25*CH_3OH + 0.95*TERPF1 + 1.03*CH_2O + HO_2	2e-12
87	$MYRCO_2 + CH_3CO_3 \rightarrow$ 0.05*MT-bRO_2 + 0.95*TERPF2 + HO_2 + 0.46*CH_3COCH_3 + 0.42*CH_2O + CH_3O_2 + CO_2	2e-12* exp(500/T)
88	$MYRCO_2 + CH_3O_2 \rightarrow$ 0.05*MT-bRO_2 + 0.25*CH_3OH + 0.95*TERPF2 + 0.75*CH_2O + HO_2	2e-12
89–91	MT-bRO_2 \ MT-cRO_2 \ MT-HOM-RO_2 + $CH_3O_2 \rightarrow$ 0.15*CH_3OH + 0.85*CH_2O + 1.4*HO_2 + 0.7*HYDRALD + 0.7*CH_3COCH_3 + 0.15*C_{10}-ROH + 0.15*C_{10}-CBYL	3.56e-14* exp(708/T)
92–94	MT-bRO_2 \ MT-cRO_2 \ MT-HOM-RO_2 + $CH_3CO_3 \rightarrow$ 0.7*CH_3O_2 + 0.7*HO_2 + 0.7*HYDRALD + 0.7*CH_3COCH_3 + 0.3*CH_3COOH + 0.15*C_{10}-ROH + 0.15*C_{10}-CBYL	7.4e-13* exp(765/T)

5. MT-RO_2 reactions with NO/NO_3

As shown in Table S6, the reactions between original MT-aRO_2 and NO/NO_3 are modified based on Xu et al. (2022) to consider the branch to form MT-bRO_2. The rate constants remain unchanged. The MT-

bRO_2\MT-cRO_2 + NO reactions are similar as the default MT-aRO_2 + NO reactions. The MT-bRO_2\MT-cRO_2 + NO_3\HO_2 reactions are based on Xu et al. (2022).

Table S6. MT-RO_2 reactions with NO/NO_3

Index	Reactions	Reaction rate
95	$APINO_2$ + NO → 0.05*MT-bRO_2 + 0.0095*TERPHFN + 0.019*TERPNS1 + 0.095*TERPNS + 0.0475*TERPNT + 0.0475*TERPNT1 + 0.77*NO_2 + 0.77*HO_2 + 0.285*TERPA + 0.2565*TERPA3 + 0.09*CH_3COCH_3 + 0.0855*TERPF1 + 0.21*CH_2O + 0.1045*TERP1OOH	2.7e-12*exp(360/T)
96	$APINO_2$ + NO_3 → 0.05*MT-bRO_2 + NO_2 + HO_2 + 0.3705*TERPA + 0.3325*TERPA3 + 0.12*CH_3COCH_3 + 0.114*TERPF1 + 0.27*CH_2O + 0.133*TERP1OOH	2.3e-12
97	$BPINO_2$ + NO → 0.05*MT-bRO_2 + 0.08*CH_3COCH_3 + 0.49*CH_2O + 0.19*TERPF1 + 0.228*TERPK + 0.038*TERPNS1 + 0.019*TERPNS + 0.057*TERPNT + 0.1235*TERPNT1 + 0.2945*TERPA3 + 0.75*HO_2 + 0.75*NO_2	2.7e-12*exp(360/T)
98	$BPINO_2$ + NO_3 → 0.05*MT-bRO_2 + 0.11*CH_3COCH_3 + 0.65*CH_2O + 0.2565*TERPF1 + 0.304*TERPK + 0.3895*TERPA3 + HO_2 + NO_2	2.3e-12
99	$LIMONO_2$ + NO → 0.05*MT-bRO_2 + 0.1615*TERPNT1 + 0.057*TERPNS1 + 0.77*NO_2 + 0.7315*TERPF1 + 0.77*HO_2 + 0.43*CH_2O	2.7e-12*exp(360/T)
100	$LIMONO_2$ + NO_3 → 0.05*MT-bRO_2 + NO_2 + 0.95*TERPF1 + HO_2 + 0.56*CH_2	2.3e-12
101	$MYRCO_2$ + NO → 0.05*MT-bRO_2 + 0.095*TERPNS1 + 0.1805*TERPNT1 + 0.71*NO_2 + 0.6745*TERPF2 + 0.33*CH_3COCH_3 + 0.3*CH_2O + 0.71*HO_2	2.7e-12*exp(360/T)
102	$MYRCO_2$ + NO_3 → 0.05*MT-bRO_2 + NO_2 + 0.95*TERPF2 + 0.46*CH_3COCH_3 + 0.42*CH_2O + HO_2	2.3e-12
103–104	MT-bRO_2\MT-cRO_2 + NO → 0.01*TERPHFN + 0.02*TERPNS1 + 0.1*TERPNS + 0.05*TERPNT + 0.05*TERPNT1 + 0.77*NO_2 + 0.77*HO_2 + 0.3*TERPA + 0.27*TERPA3 + 0.09*CH_3COCH_3 + 0.09*TERPF1 + 0.21*CH_2O + 0.11*TERP1OOH	2.7e-12*exp(360/T)
105	MT-bRO_2+ NO_3 → HO_2 + NO_2 + 0.3*C_{10}-CBYL + 0.7*HYDRALD + 0.7*ROH	1.2e-12
106	MT-cRO_2 + NO_3 → HO_2 + NO_2 + 0.75*C_{10}-CBYL + 0.25*MT-HOM-RO_2	1.2e-12
107–108	MT-bRO_2\MT-cRO_2 + HO_2 → 0.06*CH_3COCH_3 + 0.06*TERPF1 + 0.08*CH_2O + 0.25*TERP1OOH + 0.48*HO_2 + 0.4*TERPOOH + 0.29*TERPA + 0.35*OH	2.6e-13*exp(1300/T)

6. C_{10} HOMs formation

When MT-HOM-RO_2 are oxidized by HO_2\NO\$NO_3$, three kinds of gas-phase C_{10} HOMs are formed: two kinds of C_{10} non-nitrate HOMs (C_{10}-aNON and C_{10}-bNON) and C_{10} nitrate HOMs (C_{10}-ON), as shown in Table S7. The rate constants are the same as MT-RO_2 + HO_2\NO\$NO_3$ reactions in Xu et al. (2022).

Table S7. C_{10} HOMs formation

Index	Reactions	Reaction rate
109	MT-HOM-RO_2 + HO_2 → C_{10}-aNON + O_2	1.5e-11
110	MT-HOM-RO_2 + NO → 0.8*NO_2 + 0.8*HO_2 + 0.4*C_{10}-bNON + 0.8*HYDRALD + 0.2*C_{10}-ON	4.0e-12
111	MT-HOM-RO_2 + NO_3 → HO_2 + NO_2 + 0.5*C_{10}-bNON + HYDRALD	1.2e-12

7. Photolysis

Only particle-phase C_{10} HOMs undergo photolysis process (Table S8). The photolysis rate of C_{10} HOMs is fast and set as about 1/60 of NO_2 photolysis rate (Xu et al., 2022).

Table S8. Photolysis of particle-phase C_{10} HOMs (HOMs-SOA)

Index	reactions	rate constant
112–117	C_{10}-aNON\ C_{10}-bNON\ C_{10}-ON (particle phase) + hv →	0.017*jno2

8. Chemical loss of intermediate products

Three kinds of intermediate products (C_{10}-CBYL, C_{10}-ROH, and ROH) will react with OH radical (Table S9). Among them, C_{10}-CBYL and C_{10}-ROH will be transferred into MT-RO_2. The rate constant is the same as Xu et al. (2022).

Table S9. Chemical loss of C_{10}-CBYL and C_{10}-ROH

Index	Reactions	Reaction rate
118	C_{10}-CBYL + OH → 0.125*$APINO_2$ + 0.125*$BPINO_2$ + 0.125*$MYRCO_2$ + 0.125*$LIMONO_2$ + 0.475*MT-bRO_2 + 0.025*MT-cRO_2	4.6e-12*exp(70/T)
119	C_{10}-ROH + OH → 0.125*$APINO_2$ + 0.125*$BPINO_2$ + 0.125*$MYRCO_2$ + 0.125*$LIMONO_2$ + 0.475*MT-bRO_2 + 0.025*MT-cRO_2	4.6e-12*exp(70/T)
120	ROH + OH → HO_2 + CH_3COCH_3	4.6e-12*exp(70/T)

9. Wet and dry deposition of newly added species

All the newly added SOAG and SOA follows the same deposition processes with the original SOA and SOAG in VBS approach. ROH and MT-RO_2 do not go through both wet and dry deposition processes. The C_{10}-CBYL and C_{10}-ROH are dry and wet deposited using the same parameters as acetic acid (Xu et al., 2022).

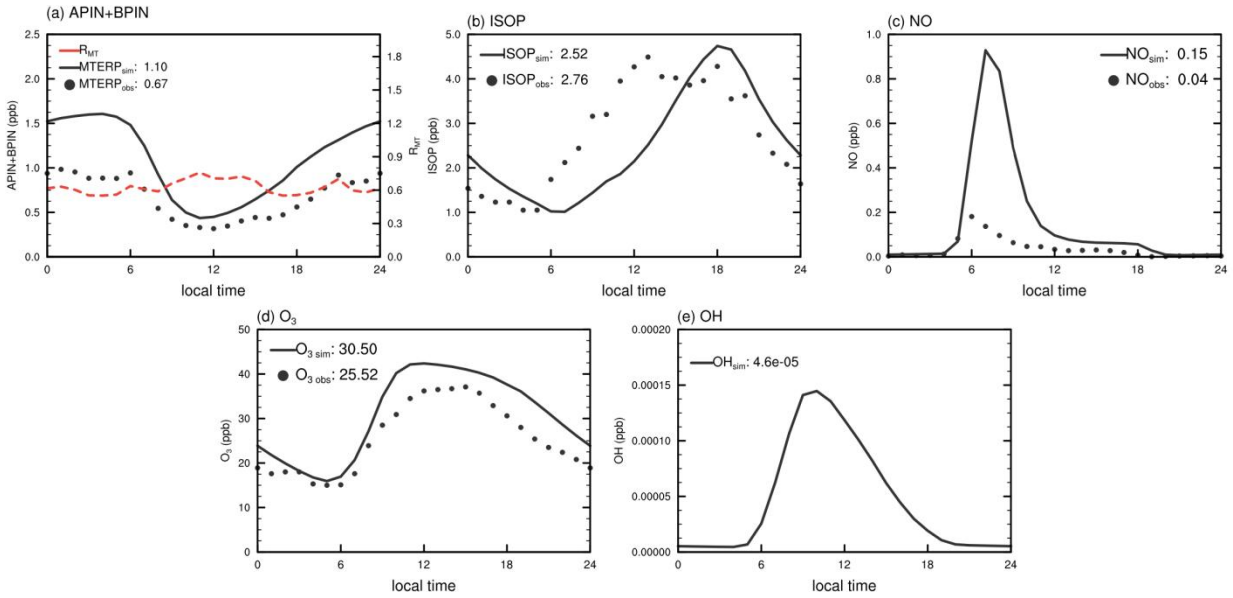

Figure S1. The diurnal cycle of simulated (black solid lines) and observed (black dots) surface (a) monoterpenes, (b) isoprene, (c) NO, (d) O_3, and (e) OH radical concentrations at the Centreville site. The ratio of the observed monoterpenes to the simulated monoterpenes (R_{MT}) are shown in red dashed line.

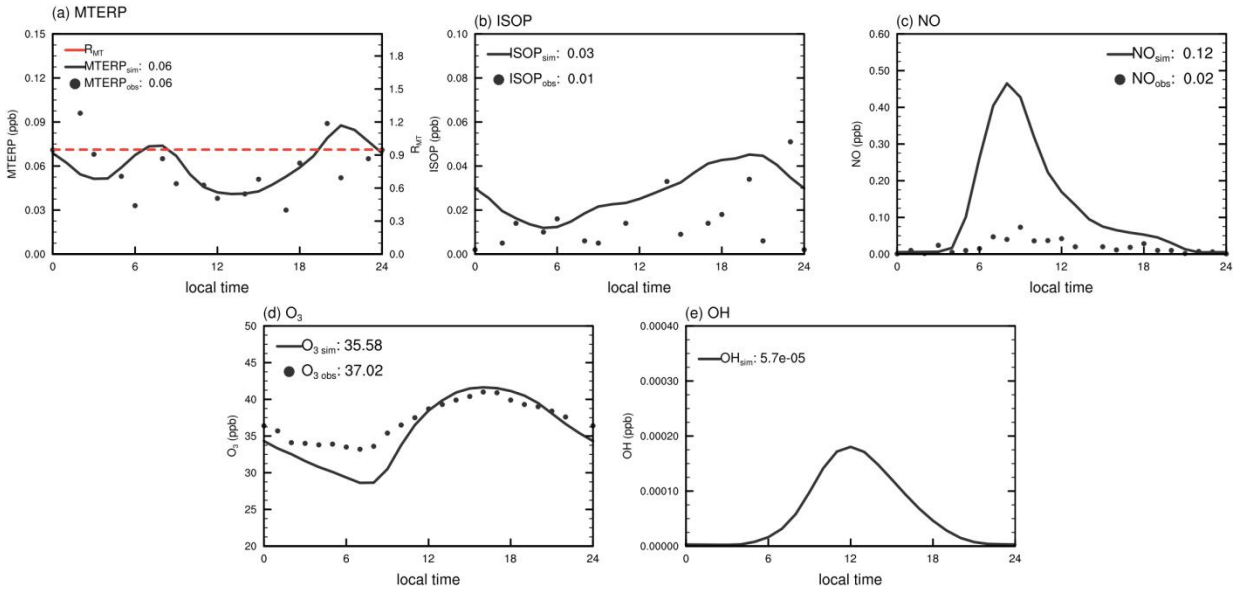

Figure S2. Same as Figure S1, but at the SMEAR II site.

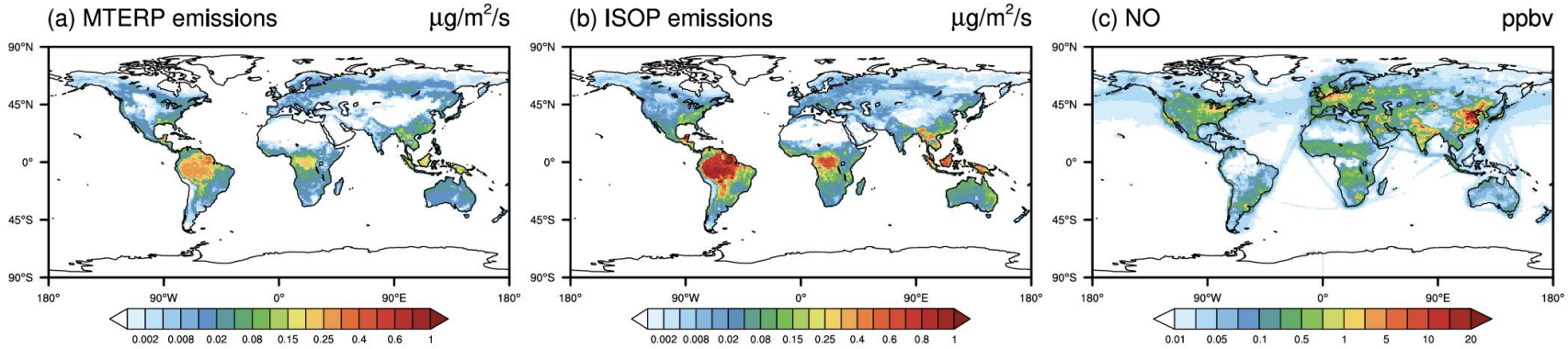

Figure S3. 2013 annual averaged surface (a) MTERP emissions (unit: µg/m^3/s), (b) ISOP emissions (unit: µg/m^3/s), (c) NO concentration (unit: ppbv) in Control experiment.

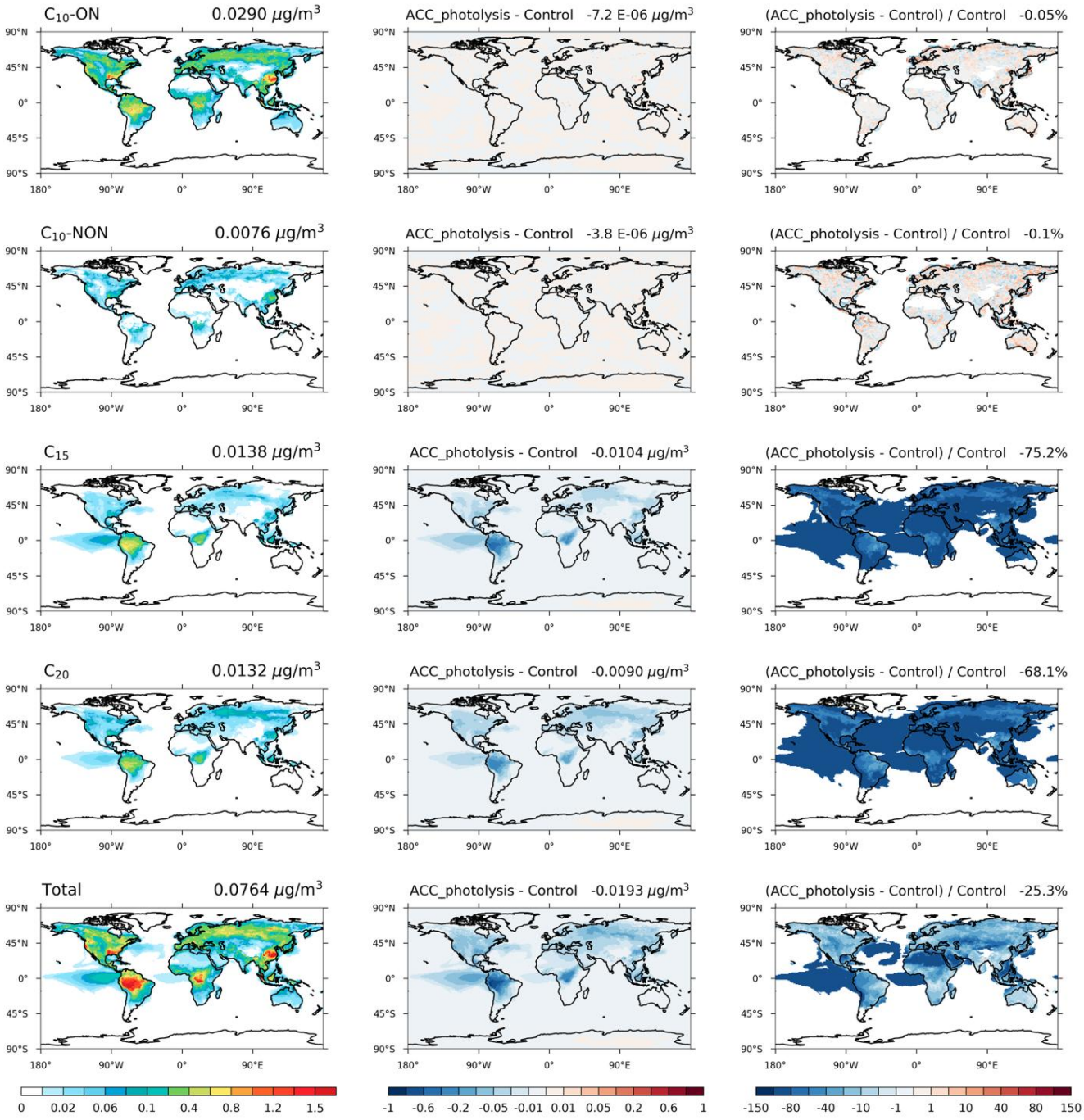

Figure S4. Global distributions of particle-phase HOMs in the control simulation (left column), the absolute changes due to accretion product photolysis (ACC_photolysis - Control; middle column), and the relative changes (right column). Each row represents a specific HOM category: C_{10}-ON, C_{10}-NON, C_{15}, C_{20}, and the total. Proportions are only shown in regions where MTSOA or total SOA is greater than 10% of the global average.

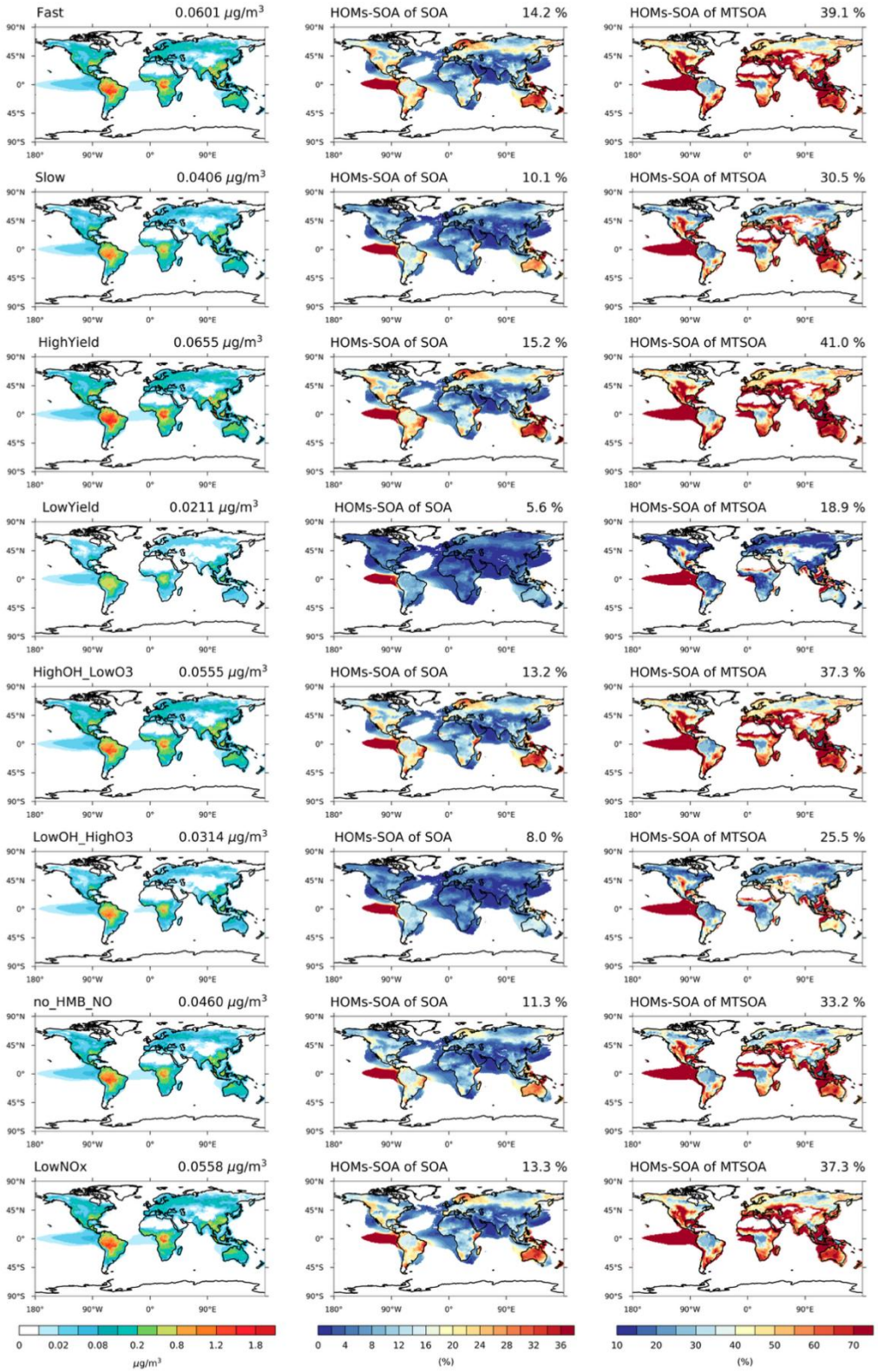

Figure S5. Global distribution of HOMs-SOA concentrations (μg/m³) and their contributions to SOA (middle column) and MTSOA (right column) across different sensitivity experiments. The global average value is displayed in the upper right corner of each panel. Proportions are only shown in regions where MTSOA or total SOA is greater than 10% of the global average.

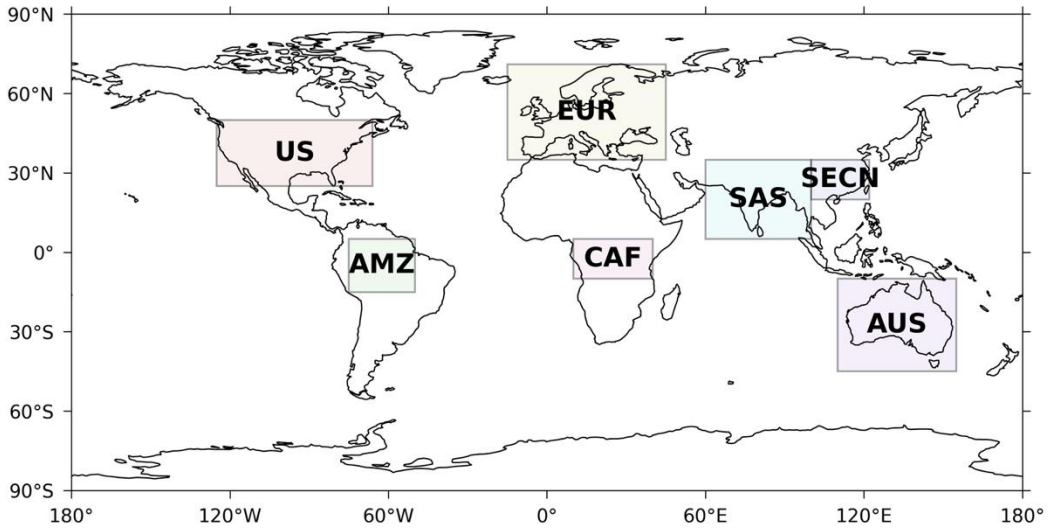

Figure S6. Map showing the geographic locations of different regions analyzed in this study: Amazon Basin (AMZ), Continental U.S. (US), Southeastern China (SECN), Europe (EUR), Australia (AUS), South Asia (SAS), Central Africa (CAF).

Table S10. Mass yield of SOAG at five traditional VBS bins.

VOCs	Oxidations	SOAG0	SOAG1	SOAG2	SOAG3	SOAG4
Isoprene	O_3				0.0033	
	NO_3				0.059024	0.025024
Monoterpenes	O_3	0.0508	0.1149	0.0348	0.0554	0.1278
	OH (low NO_x)	0.0508	0.1149	0.0348	0.0554	0.1278
	OH (high NO_x)	0.0245	0.0082	0.0772	0.0332	0.13
	NO_3^-				0.17493	0.59019
β-caryophyllene surrogate sesquiterpene	O_3	0.2202	0.2067	0.0653	0.1284	0.114
	OH (low NO_x)	0.2202	0.2067	0.0653	0.1284	0.114
	OH (high NO_x)	0.1279	0.1792	0.0676	0.079	0.1254
	NO_3				0.17493	0.59019
Glyoxal	OH	1.0				
IVOC	OH (low NO_x)	0.2381	0.1308	0.0348	0.0076	0.0113
	OH (high NO_x)	0.1056	0.1026	0.0521	0.0143	0.0166
SVOC	OH	0.5931	0.1534	0.0459	0.0085	0.0128
Benzene	OH (low NO_x)	0.0023	0.0008	0.0843	0.0443	0.1621
	OH (high NO_x)	0.0097	0.0034	0.1579	0.0059	0.0536
Toluene	OH (low NO_x)	0.1364	0.0101	0.0763	0.2157	0.0738
	OH (high NO_x)	0.0154	0.0452	0.0966	0.0073	0.238
Xylenes	OH (low NO_x)	0.1677	0.0174	0.086	0.0512	0.1598
	OH (high NO_x)	0.0063	0.0237	0.0025	0.011	0.1185

Table S11. Species for HOMs-SOA formation mechanism.

Species	Molecular formula	Description
APIN [b]	$C_{10}H_{16}$	α-pinene
BPIN [b]	$C_{10}H_{16}$	β-pinene
LIMON [b]	$C_{10}H_{16}$	Limonene
MYRC [b]	$C_{10}H_{16}$	Myrcene
$APINO_2$ [b]	$C_{10}H_{17}O_3$	peroxy radical from OH +α-pinene reaction
$BPINO_2$ [b]	$C_{10}H_{17}O_3$	peroxy radical from OH +β-pinene reaction
$LIMONO_2$ [b]	$C_{10}H_{17}O_3$	peroxy radical from OH + limonene
$MYRCO_2$ [b]	$C_{10}H_{17}O_3$	peroxy radical from OH + myrcene
$ISOPB1O_2$ [b]	$C_5H_9O_3$	OH-1-O_2-2--isoprene hydroxy peroxy radical
$ISOPZD1O_2$ [b]	$C_5H_9O_3$	OH-1-O_2-4-Z--isoprene hydroxy peroxy radical
$ISOPZD4O_2$ [b]	$C_5H_9O_3$	OH-4-O_2-1-Z--isoprene hydroxy peroxy radical
$ISOPED1O_2$ [b]	$C_5H_9O_3$	OH-1-O_2-4-E--isoprene hydroxy peroxy radical
$ISOPED4O_2$ [b]	$C_5H_9O_3$	OH-4-O_2-1-E--isoprene hydroxy peroxy radical
$ISOPB4O_2$ [b]	$C_5H_9O_3$	OH-4-O_2-3--isoprene hydroxy peroxy radical
MT-bRO_2 [a]	$C_{10}H_{16}O_4$	RO_2 from monoterpene+O_3/OH that can undergo autoxidation
MT-cRO_2 [a]	$C_{10}H_{16}O_6$	RO_2 from MT-bRO_2 autoxidation
MT-HOM-RO_2 [a]	$C_{10}H_{16}O_8$	RO_2 from MT-cRO_2 autoxidation
C_{10}-aNON [a]	$C_{10}H_{14}O_9$	gas-phase C_{10} HOMs product without nitrate from HO_2 reaction
C_{10}-bNON [a]	$C_{10}H_{14}O_9$	gas-phase C_{10} HOMs product without nitrate from NO and NO_3 reaction
C_{10}-ON [a]	$C_{10}H_{14}O_9N$	gas-phase C_{10} HOMs product with nitrate from NO reaction
SOAGac15 [a]	$C_{15}H_{18}O_7$	gas-phase C_{15} accretion product from isoprene-derived RO_2 (ISOP-RO_2) + MT-RO_2
SOAGac20 [a]	$C_{20}H_{32}O_8$	gas-phase C_{20} accretion product from MT-RO_2 + MT-RO_2
C_{10}-aNON (particle phase)	$C_{10}H_{14}O_9$	particle-phase C_{10} HOMs product without nitrate from HO_2 reaction
C_{10}-bNON (particle phase)	$C_{10}H_{14}O_9$	particle-phase C_{10} HOMs product without nitrate from NO and NO_3 reaction
C_{10}-ON (particle phase)	$C_{10}H_{14}O_9N$	particle-phase C_{10} HOMs product with nitrate from NO reaction
C_{15} (particle phase)	$C_{15}H_{18}O_7$	particle-phase C_{15} accretion product from isoprene-derived RO_2 (ISOP-RO_2) + MT-RO_2-
C_{20} (particle phase)	$C_{20}H_{32}O_8$	particle-phase C_{20} accretion product from MT-RO_2 + MT-RO_2
ROH [a]	C_3H_8O	lumped alcohols with more than 2 carbons
C_{10}-CBYL [a]	$C_{10}H_{17}O_3$	Carbonyl with 10 carbon atoms
C_{10}-ROH [a]	$C_{10}H_{17}O_3$	Alcohol with 10 carbon atoms
BIGALK	C_5H_{12}	lumped alkanes C>3
CO [b]	CO	carbon monoxide
CO_2 [b]	CO_2	carbon dioxide
CH_2O [b]	CH_2O	formaldehyde
CH_3O_2 [b]	CH_3O_2	methylperoxy radical
CH_3CO_3 [b]	CH_3CO_3	acetylperoxy radical
CH_3COCH_3 [b]	CH_3COCH_3	acetone
CH_3COOH [b]	CH_3COOH	acetic acid
CH_3OH [b]	CH_3OH	methanol
HO_2 [b]	HO_2	hydroperoxyl radical

H_2O_2 [b]	H_2O_2	hydrogen peroxide
HCOOH [b]	HCOOH	formic acid
HMHP [b]	CH_4O_3	hydroxy methyl hydroperoxide
HYAC [b]	CH_3COCH_2OH	hydroxyacetone
HYDRALD [b]	$HOCH_2CCH_3CHCHO$	lumped unsaturated hydroxycarbonyl
TERP1OOH [b]	$C_{10}H_{18}O_3$	terpene-derived hydroxy hydroperoxide with 1 double bond
TERPA [b]	$C_{10}H_{16}O_2$	aldehyde terpene product with no double bonds that contains a ring like pinonaldehyde
TERPACID [b]	$C_{10}H_{16}O_4$	carboxylic acid/peracid from TERPA
TERPA2 [b]	$C_9H_{14}O_2$	TERPA oxidation product with no double bonds that contains an aldehydic group
TERPA2O_2 [b]	$C_9H_{15}O_4$	TERPA peroxy radical 2nd step
TERPA2CO_3 [b]	$C_9H_{13}O_4$	acyl peroxy radical from TERPA2
TERPA3 [b]	$C_9H_{14}O_3$	aldehyde terpene product with no ring like limonaldehyde
TERPA3CO_3 [b]	$C_9H_{13}O_5$	acyl peroxy radical from TERPA3
TERPF1 [b]	$C_{10}H_{16}O_2$	functionalized terpene product with 1 double bond typically containing carbonyl groups
TERPF2 [b]	$C7H_{10}O$	functionalized terpene product with 2 double bonds typically containing carbonyl groups
TERPHFN [b]	$C_{10}H_{19}NO_7$	terpene highly functionalized nitrate
TERPK [b]	$C_9H_{14}O$	terpene product containing a ketone group
TERPNS [b]	$C_{10}H_{17}NO_4$	terpene-derived saturated secondary or primary nitrate
TERPNS1 [b]	$C_{10}H_{17}NO_4$	terpene-derived unsaturated secondary or primary nitrate
TERPNT [b]	$C_{10}H_{17}NO_4$	terpene-derived saturated tertiary nitrate
TERPNT1 [b]	$C_{10}H_{17}NO_4$	terpene-derived unsaturated tertiary nitrate

[a] Xu et al. (2022)

[b] Schwantes et al. (2020)

Table S12. The Normalized Mean Bias (NMB), Correlation Coefficient (R), and Root Mean Square Error (RMSE) values of C_{10}-HOMs (C_{10}-ON+C_{10}-NON) comparing two sites with observations. Site and field campaign information can be found in Table 7.

	Hyytiälä site			**Centreville site**		
	NMB (%)	R	RMSE (ng/m^3)	NMB (%)	R	RMSE (ng/m^3)
HighOH_LowO3	77	0.65	74	119	0.87	476
LowOH_HighO3	-46	0.06	43	-25	0.41	135
Fast	96	0.66	93	141	0.87	576
Slow	-21	0.17	30	23	0.39	148
No_HMB_NO	3	0.45	24	57	0.39	259
HighYield	77	0.65	74	119	0.87	476
LowYield	-69	0.59	59	-62	0.86	220
LowNOx	70	0.60	67	2	0.40	111
Control	69	0.61	66	121	0.74	497

Table S13. The global averaged value of 2013 annual mean surface HOMs-SOA (unit: μg/m3), the contribution of HOMs-SOA to the total MTSOA and the contribution of HOMs-SOA to the total SOA (unit: %) using different sensitivity tests (Table 8).

Experiment	**HOMs-SOA (μg/m^3)**	**HOMs-SOA / Total SOA**	**HOMs-SOA / MTSOA**
Control	0.056	11%	37%
LowYield	0.021	6%	19%
HighYield	0.066	15%	41%
HighOH_lowO3	0.056	13%	37%
LowOH_HighO3	0.031	8%	26%
Fast	0.060	14%	39%
Slow	0.041	10%	31%
no_HMB_NO	0.046	11%	33%
LowNOx	0.056	13%	37%

Table S14. Molecular formulas of top 5 contributing HOM-ON and HOM-NON species (gas- and particle-phase) at Centreville, Alabama

HOM-ON		HOM-NON	
Gas-phase	**Particle-phase**	**Gas-phase**	**Particle-phase**
C10H15O7N1	C10H15O7N1	C10H14O7	C10H14O7
C10H17O7N1	C10H15O8N1	C10H12O7	C10H12O7
C10H15O8N1	C10H17O7N1	C10H22O8	C10H16O7
C10H17O8N1	C10H17O8N1	C10H22O7	C10H22O8
C10H13O8N1	C10H15O9N1	C10H16O7	C10H22O7

Table S15. Molecular formulas of top 5 contributing HOM-ON and HOM-NON species (gas- and particle-phase) at Hyytiälä, Finland

HOM-ON		HOM-NON	
Gas-phase	**Particle-phase**	**Gas-phase**	**Particle-phase**
C10H15O7N1	C10H15O8N1	C10H12O11	C10H14O7
C10H15O8N1	C10H15O7N1	C10H14O8	C10H22O9
C10H17O7N1	C10H17O7N1	C10H16O8	C10H22O7
C10H13O7N1	C10H17O8N1	C10H14O7	C10H22O8
C10H17O8N1	C10H15O9N1	C10H22O7	C10H16O7

Reference

Berndt, T., et al. (2016), Hydroxyl radical-induced formation of highly oxidized organic compounds, Nat Commun, 7, 13677, doi: 10.1038/ncomms13677.

Ehn, M., et al. (2014), A large source of low-volatility secondary organic aerosol, Nature, 506(7489), 476-479, doi: 10.1038/nature13032.

Jokinen, T., et al. (2015), Production of extremely low volatile organic compounds from biogenic emissions: Measured yields and atmospheric implications, Proc Natl Acad Sci U S A, 112(23), 7123-7128, doi: 10.1073/pnas.1423977112.

Lee, B. H., S. Iyer, T. Kurtén, J. G. Varelas, J. Luo, R. J. Thomson, and J. A. Thornton (2023), Ring-opening yields and auto-oxidation rates of the resulting peroxy radicals from OH-oxidation of α-pinene and β-pinene, Environmental Science: Atmospheres, 3(2), 399-407, doi: 10.1039/d2ea00133k.

Moller, K. H., R. V. Otkjaer, J. Chen, and H. G. Kjaergaard (2020), Double Bonds Are Key to Fast Unimolecular Reactivity in First-Generation Monoterpene Hydroxy Peroxy Radicals, J Phys Chem A, 124(14), 2885-2896, doi: 10.1021/acs.jpca.0c01079.

Nah, T., J. Sanchez, C. M. Boyd, and N. L. Ng (2016), Photochemical Aging of alpha-pinene and beta-pinene Secondary Organic Aerosol formed from Nitrate Radical Oxidation, Environ Sci Technol, 50(1), 222-231, doi: 10.1021/acs.est.5b04594.

Piletic, I. R., and T. E. Kleindienst (2022), Rates and Yields of Unimolecular Reactions Producing Highly Oxidized Peroxy Radicals in the OH-Induced Autoxidation of alpha-Pinene, beta-Pinene, and Limonene, J Phys Chem A, 126(1), 88-100, doi: 10.1021/acs.jpca.1c07961.

Pye, H. O. T., et al. (2019), Anthropogenic enhancements to production of highly oxygenated molecules from autoxidation, Proc Natl Acad Sci U S A, 116(14), 6641-6646, doi: 10.1073/pnas.1810774116.

Roldin, P., et al. (2019), The role of highly oxygenated organic molecules in the Boreal aerosol-cloud-climate system, Nat Commun, 10(1), 4370, doi: 10.1038/s41467-019-12338-8.

Schervish, M., and N. M. Donahue (2020), Peroxy radical chemistry and the volatility basis set, Atmospheric Chemistry and Physics, 20(2), 1183-1199, doi: 10.5194/acp-20-1183-2020.

Schwantes, R. H., et al. (2020), Comprehensive isoprene and terpene gas-phase chemistry improves simulated surface ozone in the southeastern US, Atmospheric Chemistry and Physics, 20(6), 3739-3776, doi: 10.5194/acp-20-3739-2020.

Weber, J., S. Archer-Nicholls, P. Griffiths, T. Berndt, M. Jenkin, H. Gordon, C. Knote, and A. T. Archibald (2020), CRI-HOM: A novel chemical mechanism for simulating highly oxygenated organic molecules (HOMs) in global chemistry–aerosol–climate models, Atmospheric Chemistry and Physics, 20(18), 10889-10910, doi: 10.5194/acp-20-10889-2020.

Xu, L., K. H. Moller, J. D. Crounse, R. V. Otkjaer, H. G. Kjaergaard, and P. O. Wennberg (2019), Unimolecular Reactions of Peroxy Radicals Formed in the Oxidation of alpha-Pinene and beta-Pinene by Hydroxyl Radicals, J Phys Chem A, 123(8), 1661-1674, doi: 10.1021/acs.jpca.8b11726.

Xu, R., J. A. Thornton, B. H. Lee, Y. Zhang, L. Jaeglé, F. D. Lopez-Hilfiker, P. Rantala, and T. Petäjä (2022), Global simulations of monoterpene-derived peroxy radical fates and the distributions of highly oxygenated organic molecules (HOMs) and accretion products, Atmospheric Chemistry and Physics, 22(8), 5477-5494, doi: 10.5194/acp-22-5477-2022.

Yan, C., et al. (2016), Source characterization of highly oxidized multifunctional compounds in a boreal forest environment using positive matrix factorization, Atmospheric Chemistry and Physics, 16(19), 12715-12731, doi: 10.5194/acp-16-12715-2016.